Hydration-induced stiffness enabling robust thermal cycling of high temperature fuel cells cathode

Hongxin Yang[1], Yuan Zhang[2,3] ✉, Zhipeng Liu[1], Chunfang Hu[1], Junbiao Li[1], Hailong Liao[1], Minhua Shao [2,4], Meng Ni [5], Bin Chen [1] ✉, Zongping Shao [6] ✉ & Heping Xie [1] ✉

Thermo-mechanics of cathode is closely related to the durability of high-temperature solid oxide fuel cells (SOFCs), with two main mechanical failures during thermal cycling: interface delamination and bulk cracking of cathode. Bulk cracking, caused by insufficient fracture strength/stiffness is a big concern but often overlooked. Here, we introduce chemical hydration to offset the thermal expansion, enhancing the cathodic mechanical stiffness and fracture strength, thus promoting the thermo-mechanical durability of cathode in proton ceramic fuel cells (PCFCs). Such chemical-induced expansion offset is achieved by strengthening intergranular bonding inside the bulk cathode after the hydration, preventing granule detachment during thermal shrinkage. As a demonstration, the stiffness-enhanced air electrode ($BaCo_{0.7}Ce_{0.15}Y_{0.15}O_3$, noted as s-BCC-Y) exhibits 86% enhancement of fracture strength, thus thermal cycling stability with almost no degradation after 35 harsh thermal cycles between 600 and 300 °C, surpassing pristine $BaCo_{0.7}Ce_{0.3}O_3$ and many cobalt-free PCFC cathodes. Benefitted from the improved stiffness of cathode, full cell with the s-BCC-Y electrode demonstrates enhanced power output. This work highlights the importance of bulk cathode thermo-mechanics in developing robust SOFCs for high temperature energy applications.

Solid oxide fuel cells (SOFCs) can directly convert the chemical energy of fuels into electrical energy. Their high energy conversion efficiency and environmental friendliness align well with current trends in energy markets for higher sustainability. At high operating temperatures (i.e., above 600 °C), their overall efficiency could exceed 80%. Unfortunately, the high-temperature operation brings challenges to the industrialization of SOFCs, including multiple degradation issues at levels and scales from particle to system, especially during thermal

[1]State Key Laboratory of Intelligent Construction and Healthy Operation and Maintenance of Deep Underground Engineering, Guangdong Provincial Key Laboratory of Deep Earth Sciences and Geothermal Energy Exploitation and Utilization, College of Civil and Transportation Engineering, Shenzhen University, Shenzhen, China. [2]CIAC-HKUST Joint Laboratory for Hydrogen Energy, The Hong Kong University of Science and Technology, Clear Water Bay, Kowloon, Hong Kong, China. [3]Graphene Composite Research Center, College of Chemistry and Environmental Engineering, Shenzhen University, Shenzhen, China. [4]Guangzhou Key Laboratory of Electrochemical Energy Storage Technologies, Fok Ying Tung Research Institute, The Hong Kong University of Science and Technology, Guangzhou, China. [5]Department of Building and Real Estate, Research Institute for Sustainable Urbanization (RISUD) and Research Institute for Smart Energy (RISE), The Hong Kong Polytechnic University, Hung Hom, Hong Kong, China. [6]WA School of Mines: Minerals, Energy and Chemical Engineering, Curtin University, Perth, WA, Australia. ✉e-mail: yuanzhang1216@szu.edu.cn; chenbin@szu.edu.cn; zongping.shao@curtin.edu.au; xiehp@szu.edu.cn

cycling[1,2]. In particular, the performance degradation of air electrodes (also called cathodes) is largely attributed to mechanical failures including interface delamination and bulk cracking[3]. Early studies have been aimed at solving the interface delamination issue, through the reduction of the thermal expansion coefficient (TEC) of cathodes to match with the rigid electrolyte[4]. For example, developing low Co or Co-free cathode[5], compositing with the electrolyte powder[6–10], or negative thermal expansive addictive[3,11] were all proven to be effective (description in details in SI-1). However, merely reducing the TEC may not fulfill all the thermal-mechanical requirements of a robust cathode since the bulk crack issue of the cathode remains.

Principally, the porous cathode is the most vulnerable layer to mechanical cracks in the membrane-electrode assembly (MEA) of SOFC due to its low fracture strength, originating from its high grain boundary embrittlement. In anode-supported SOFC, the cathode layer is normally prepared by co-firing with anode substrate at ~900–1200 °C, lower than the sintering temperature of the dense electrolyte layer alone (>1300 °C). The contact bonding of cathode grains is therefore substantially lower in strength than that of the electrolyte layer or the anode later. For example, the classic fracture strength of 8YSZ[12] and $BaZr_{0.1}Ce_{0.7}Y_{0.1}Yb_{0.1}O_{3-\delta}$ (BZCYYb) is respectively 145 and 84.43 MPa (measured in this work), much higher than that of bench-marking cathodes, i.e., 34 MPa for BSCF[13] and 40 MPa for LSCF[14]. Therefore, during both cathode layer fabrication (i.e., cooling process after the firing) and operation (i.e., thermal cycling between room temperature and working temperature), the bulk cracks are more likely to occur in cathode layer than other layers, when the cell is subjected to internal thermal stress and external mechanical loading. Particularly in practical operation of large-size SOFC in stacks, large compression load is needed to ensure good current collecting, which could cause cracks in cathode due to the press-in of interconnectors[15]. To solve the bulk crack issue, the stiffness of cathode (measured by the modulus and hardness) and mechanical strength that are jointly determined by the grain contacting strength and mechanical expansion behavior, need to be improved[16,17]. But unfortunately, this has been long-time overlooked.

Here, we took the state-of-art triple conducting $BaCo_{0.7}Ce_{0.3}O_3$ (BCC)[18,19] as a parent perovskite material for the development of cathode, which was selected because of it high oxygen reduction reaction (ORR) activity, but it also unfavorably high TEC and low bulk stiffness and fracture strength (~28 MPa). We further proposed a chemical-induced expansion offset strategy to facilely improving the stiffness and anti-crack capability of the cathode by doping Y at the B site of pristine ABO_3 structure. Characterizations indicate that the chemical-induced expansion offset originates from the Y-doping enhanced hydration of the oxide lattice, thus strengthening the intergranular bonding inside the bulk cathode by counteracting the detaching of cathode granules during the thermal shrinkage (from calcination temperature to room temperature). As a result, the stiffness-improved $BaCo_{0.7}Ce_{0.15}Y_{0.15}O_3$ (s-BCC-Y) demonstrated better material mechanical and electrochemical performance.

Results

Hydration-induced chemical expansion concept

As known, the cathode experiences significant thermal stress due to the mismatch of the TEC with the electrolyte materials, especially during temperature cycling. This thermal stress leads to interface delamination and cathode fracture. Numerical studies (SI-1) have focused on optimizing interface delamination from the perspective of TEC, while the issue of cathode fracture has been largely neglected for a long time. Figure 1a illustrates that at the calcination temperature, the cathode could be free of thermal stress with all granules well connected with neighbors. During cooling, the thermal shrinkage would cause intergranular faults, deteriorating the stiffness and thus causing cathode fracture. Supposing additional chemical expansion

during this cooling process, the faults would be alleviated and the stiffness can be restored−denoted as the concept of "hydration-induced chemical expansion offset".

To practice this concept, we used Y doping to create the desired chemical induced expansion and study its effect on the stiffness of traditional cobalt-containing perovskite since it was reported that the substitution of trivalent Y^{3+} in the B site of perovskite generally introduced significant chemical expansion (i.e., by about 73.7% from 0.019 to 0.033 expansion in $BaZr_{0.95}Y_{0.05}O_{2.975}$ and $BaZr_{0.8}Y_{0.2}O_{2.9}$)[20]. Moreover, possibly increasing oxygen vacancy, which means that oxygen ions have more pathways for transport, which facilitates the migration of oxygen ions and the reduction reaction, thereby enhancing the catalytic activity of the SOFC cathode[21–23]. The $BaCo_xCe_yO_3$[18,19] was selected as the parent perovskite as it has promising ORR/(oxygen evolution reaction) OER activity due to its high triple-conducing properties and stability in water-containing atmosphere, while its TEC is still too high to maintain good thermo-mechanical robustness. As schemed in Fig. 1b at the granule/lattice level, Y^{3+} doped BCC (s-BCC-Y) perovskite is expected to generate more oxygen vacancies for enhanced hydration reactions, which would expand the lattice during cooling since the hydration is thermodynamically exothermic[20,24]. This lattice expansion is induced chemically by Y doping and could counteract the generation of intergranular faults.

To verify this, we first prepared s-BCC-Y ($BaCo_{0.7}Ce_{0.15}Y_{0.15}O_3$) and BCC by a facile sol-gel method by calcination at 1000 °C in air. X-ray diffraction (XRD) patterns of the parent BCC and as-obtained s-BCC-Y were observed at room temperature, as shown in Fig. 1c, d. As expected, the s-BCC-Y material was self-assembled into two crystalline phases, a major cubic perovskite phase (89.7%, Pm-3m, $BaCo_{0.74}Ce_{0.094}Y_{0.166}O_3$) and a minor rhombohedral phase (10.3%, R-3c, $BaCo_{0.11}Ce_{0.86}Y_{0.03}O_3$) based on the Rietveld refinement (details shown in SI-2). In addition, lattice spacings were measured from this selected region, $BaCoO_3$ (102) and $BaCeO_3$ (110) in BCC, Pm-3m (100) and R-3c (110) in s-BCC-Y were clearly observed, in good accordance with the XRD refinement results, as shown in Fig. 1e, f. These refinement results correspond well with the interplanar spacings calculated from Selected area electron diffraction (SAED) pattern, and the Energy-dispersive X-ray (EDX) analysis also confirmed the presence of Co-rich and Ce-rich phases (shown in SI-3). To better present how Y affected these two phases, we conducted DFT calculations and performed iterative self-consistent cycles for structural optimization (mainly focusing on bond strength and angles). All structures were fully relaxed until the maximum force on each atom was less than 0.01 eV/Å, and the energy convergence criterion was set to 10^{-8} eV (as shown in SI-4). More importantly, it can be observed in the high resolution TEM images that the introduction of Y elements assuredly reduced the intergranular fault regions between grains, resulting in a thinner intergranular amorphous phase at grain boundaries, which was reported to be not only beneficial for both proton conduction and phase stability against decomposition at the same time[25], but also for enhancing the material's stiffness[26,27].

Based on the results above, we can confirm the successful substitution of Y in the positions of Co and Ce in the B-site of BCC. Due to the larger ion radius of Y^{3+} than Ce^{4+} (0.9 Å vs. 0.87 Å)[28], doping Y into the lattice of BCC at the synthesis temperature would create lattice expansion and more lattice oxygen vacancies, if then cooled down to room temperature, the created lattice oxygen vacancy could bring in more hydration, forming proton defects and therefore realizing the mitigation of thermal shrinking due to refill of oxygen vacancies by hydration as already widely verified in proton conducting perovskite[24,29,30]. To further validate the enhanced hydration capacity introduced by Y doping in BCC, we compared the weight changes of BCC and s-BCC-Y from 30 to 1000 °C in dry air, as shown in the TG and DTG analyses in Fig. 1g. Beyond the typical water loss in the
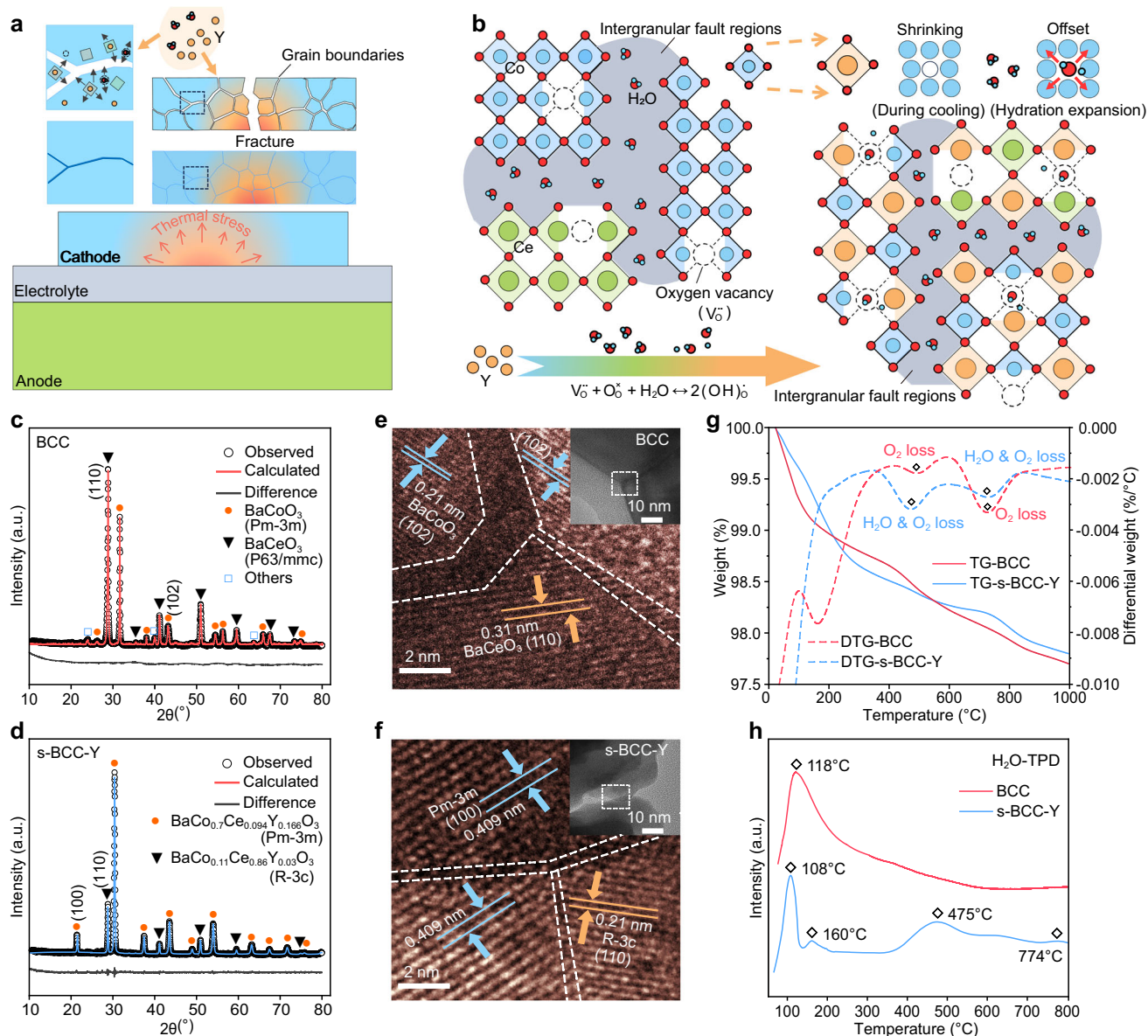
Fig. 1 | Illustrations of enhancement mechanism and material characterization. a Cathode fracture mechanisms and the influence of Y element and water molecules on grain intercontact boundary. **b** Y-doping impact on hydration expansion, vacancies, and crystal structure. Co, Ce, Y, and O, are blue, green, yellow, and red solid circles, respectively, the black hollow circles represent oxygen vacancies, and the gray area represents the intergranular fault regions between the grains. **c**, **d** are XRD patterns of BCC and s-BCC-Y powder and Rietveld refinement results. **e**, **f** represent TEM observations of lattice spacing measurement and interface between different phases within BCC and s-BCC-Y particles, respectively. **g** TG and DTG analysis of hydrated BCC and s-BCC-Y from RT to 1000 °C. **h** H_2O-TPD of BCC and s-BCC-Y from RT to 800 °C. Source data for Fig. 1c, d, g, h were provided as a Source Data file.

100–200 °C range, commonly observed in porous materials, both BCC and s-BCC-Y exhibit notable mass losses from 400 to 1000 °C, particularly around 450 °C and 750 °C. This behavior aligns with that of many cathode materials[31,32]. Extensive studies[33–35] have attributed this phenomenon primarily to the loss of lattice oxygen in perovskite cathodes, which is an indication of hydration. Therefore, the observed enhanced weight loss at 450 °C could be caused by the enhanced hydration in Y doped s-BCC-Y. Temperature-programmed desorption (TPD) tests were also conducted in water and oxygen environments to confirm the TG results. The results shown in Fig. 1h (H_2O-TPD) and SI-5 (O_2-TPD), indicate that the mass loss in BCC in TG is mainly due to loss of lattice oxygen, while s-BCC-Y' mass loss not only contributes to lattice oxygen but a significant amount of water. This observation again highlights the superior hydration capability of s-BCC-Y compared to BCC.

Reduction of TEC and interface optimization

The hydration-induced expansion is expected to mitigate the dilatometric response, as evidenced by the experimental curves of bar-shaped samples in ambient air with a slight amount of moisture. As shown in Fig. 2a. Y doping reduced the TEC of BCC by 34.1% (BCC: $25.89 \times 10^{-6} K^{-1}$, s-BCC-Y: $17.06 \times 10^{-6} K^{-1}$, in the range of 300 to 800 °C). The calculation formula for TEC and the specific experimental test data are depicted in SI-6, and the atomic coordinates of the optimized computational models were provided in our Supplementary Data 1. The ab initio Car-Pareinello molecular dynamics (AIMD) in the framework of the density functional theory (DFT)[36] was further used to validate the TEC mitigation, as marked by dotted values in Fig. 2a, where the main Co-rich phase ($BaCo_{0.74}Ce_{0.094}Y_{0.166}O_3$) of s-BCC-Y composite was simplified to $BaCo_{0.7}Y_{0.15}O_3$ for a reasonable DFT calculation
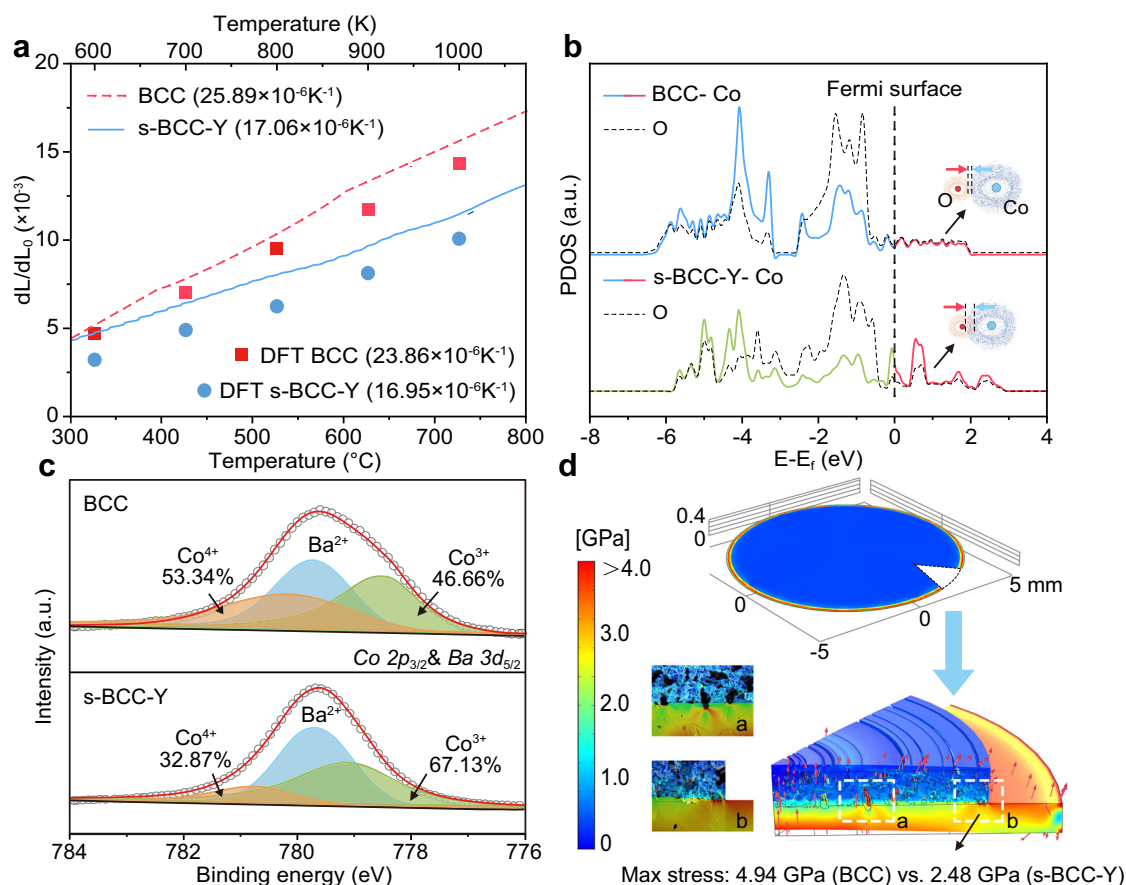
Fig. 2 | TEC evaluation, analysis, and its effect on the cathode-electrolyte interface. a TEC figure, measured by thermal dilatometer and DFT calculation results for both BCC and s-BCC-Y. **b** PDOS of Co and O elements for BCC and s-BCC-Y, and influence of Y-doping on Co-O bonds. **c** XPS for Co element of two cathode materials. **d** Numerical simulation of thermal stress at cathode-electrolyte interface, 600 °C. Source data for (**a**–**c**) were provided as a Source Data file.

time cost. The simulation expansion behavior of lattice after Y doping shows smaller changes in the lattice constant upon temperature incase (see Table S6). This reduced variation can be attributed to the influence of Y on the outer electrons of Co atoms and the strengthening of the Co-O bond energy[37,38]. Interestingly, the simulated TECs are slightly smaller than experimental values, especially for s-BCC-Y below 600 °C. Considering the simulation process of TECs by DFT calculation does not account for the hydration-induced chemical expansion, we attribute this discrepancy to the chemical expansion that offsets the thermal shrinkage when lowering the temperature. To further explain the reduction of TEC, the partial density of states (PDOS) of cubic perovskite $BaCoO_3$ and $BaCo_{0.7}Y_{0.15}O_3$ as model systems were calculated, which were commonly used to analyze changes in cathode electrochemical performance[39], as shown in Fig. 2b. Co ions show a considerable density of states around the Fermi level, indicating Co^{4+} can easily transform into Co^{3+} [40]. Specifically, a distinct resonance peak of Co and O elements was observed above the Fermi level, which means electron clouds of Co and O further overlap and suggests that the Co-O equilibrium interatomic distance (the bond length)[41] turns to be shorter. As is commonly recognized, a decrease in bond length is accompanied by an increase in bond energy[42–44]. The observed increase of Co-O bond energy after the Y doping indicates an improved resistance to thermal lattice expansion, thereby reducing the overall TEC. This trend also conforms with the calculation data obtained from DFT (SI-6, Table S6). In addition, we also validated these PDOS results by XPS characterizations. The fitted XPS plots of Co 2p3/2 in the BCC and s-BCC-Y are shown in Fig. 2c. In BCC, the Co^{3+} and

Co^{4+} are 46.66% and 53.34%, while they are 67.13% and 32.87% for s-BCC-Y, respectively. This not only confirms the analysis results from DFT, which indicates Co^{4+} can more easily transform into Co^{3+} but also indicates that the introduction of Y lowers the overall valence state of BCC. It is conducive to the formation of oxygen vacancies to enhance the ORR activity[45–48]. The Ce-rich phase was further characterized using PDOS from DFT calculations and XPS, as shown in SI-7. The PDOS results indicate that Ce's electronic states cross the Fermi level, suggesting enhanced conductivity, consistent with previous reports on the high conductivity of yttrium-doped barium zirconate[49]. XPS analysis further reveals a reduction in Ce's chemical valence, which correlates with the observed decrease in Co's chemical valence.

Although the TEC of this cathode has been significantly reduced, it still large like many other excellent cathode materials, such as BSCF[50] ($19.95 \times 10^{-6} K^{-1}$, 50–1000 °C) and BCFZY[51] ($18.38 \times 10^{-6} K^{-1}$, 400–800 °C), when compared to the electrolyte material ($9–12 \times 10^{-6} K^{-1}$). In practical engineering, TEC is only one of the important factors affecting interfacial delamination, and it is influenced by many other factors such as the thickness, porosity, and hydration level of the cathode. To quantify the beneficial effect of hydration-induced TEC mitigation, as well as the specific interfacial optimization effect brought by this degree of TEC reduction. Numerical simulations were performed to probe the interface thermal stress at a typical operating temperature (600 °C) using the Finite Element Method for a 2D-axisymmetrical model of the porous cathode coated on a dense proton conducting electrolyte (BZCYYb) based on reconstructed geometries from cross sectional SEM images. The details of simulation
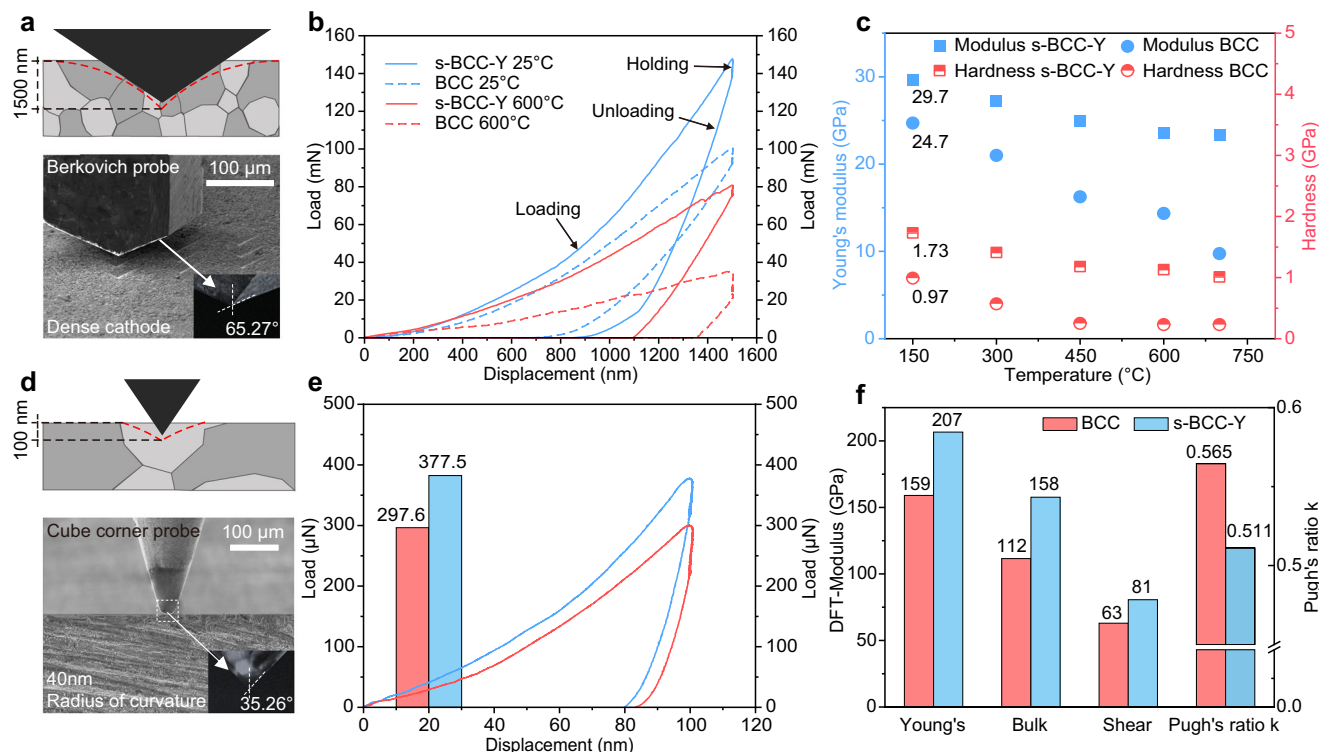
Fig. 3 | High-temperature nanoindentation test, stiffness analysis by experiment, and DFT. a Berkovich probe (half angle of 65.27°) and nanoindentation test diagram. **b** Load-displacement curves under Berkovich probe at 25 °C and 600 °C with a displacement control of 1500 nm. **c** Variation of Young's modulus and hardness with temperature during high-temperature nanoindentation. **d** Cube corner probe (half angle of 35.26°, curvature of radius 40 nm) and nanoindentation test diagram. **e** Ultra-precision nanoindentation test with cube corner probe in 100 nm. **f** Theoretical Young's, Bulk, Shear modulus, and Pugh's ratio k of BCC and s-BCC-Y calculated by DFT. Source data for (**b**, **c**, **e**) were provided as a Source Data file.

parameters were shown in SI-8. The simulated von Mises stress at the cathode-electrolyte interface revealed a clear decrease due to the mitigation of TEC. This reduction is particularly pronounced at the cathode edges, where thermal stress is concentrated, as shown in Fig. 2d. The 34.1% reduction in TEC leads to a 49.8% decrease in von Mises stress at the interface edges (from 4.94 to 2.48 GPa). These simulated results suggest that hydration-induced TEC mitigation can significantly reduce the risk of interfacial delamination between the cathode and electrolyte.

Hydration-enhanced bulk stiffness at a micro-scale
As already stated in the main, delamination is not the only cause for mechanical failure of the cathode, and bulk cracking also plays a significant role[52,53]. Particularly at high temperature, the cathode materials are more susceptible to damage and cracking due to the thermal-reduced stiffness[54,55]. Here we compared the bulk stiffness and fracture strength of the hydration-enhanced cathode after the Y doping. First, according to the definition of stiffness, Young's modulus is viewed as a key parameter to characterize it[16,17]. Therefore, high-temperature nanoindentation tests were conducted to measure the Young's modulus and hardness of the cathode. A Berkovich indenter was used for the nanoindentation test at a displacement control mode at varied temperatures (Fig. 3a), and the load-displacement curves at maximum depth to 1500 nm are shown in Fig. 3b. s-BCC-Y exhibited better resistance to the indenter intrusion. Specifically, at 25 °C, s-BCC-Y showed a maximum load of 147 μN, while BCC only displayed 98 μN. As the temperature rises to 600 °C, s-BCC-Y maintained a maximum load of 80 μN compared to 35 μN for BCC. The most commonly used analysis method for obtaining hardness and modulus was developed by Oliver and Pharr[56,57]. With their method, Young's modulus and hardness were calculated, and the results were shown in Fig. 3c and the test

curves were presented in SI-9. As expected, similar to the most ceramic perovskites, both Young's modulus and hardness decreased with increasing temperature[58,59]. As expected, s-BCC-Y always exhibited superior values, which indicates enhanced stiffness at all temperatures than BCC.

For a more detailed mechanical assessment, ultra-precision pressure sensors and Cube corner probe were used in 100 nm indentation, shown in Fig. 3d, e. Different from the Berkovich probe, which is often conducted to calculate Young's modulus and hardness of bulk samples[60,61], this Cube corner probe with a smaller half angle and a 40 nm tip curvature radius can be used to assess the stiffness of individual grains without the interference of grain boundaries. In this 100 nm indentation test, s-BCC-Y achieved a maximum load of 360.6 μN, higher than BCC (280.1 μN), further indicating that the Y-doping enhanced the stiffness of individual grain in a lattice-scale condition.

The modulus of the Co-rich ($BaCoO_3$) and Ce-rich ($BaCeO_3$) structures, as well as their Y-doped variants were also simulated by DFT calculations. The modulus calculations were conducted using VASP, with plane-wave basis sets and projector augmented-wave (PAW) pseudopotentials. Structural optimizations were performed until the maximum atomic force was reduced to less than 0.01 eV/Å, and the energy convergence criterion was set to 10^{-8} eV. Seven different strains were applied, ranging from −0.015 to 0.015 with an increment of 0.005. VASPKIT was utilized for data extraction and post-processing of the calculated results. All Voigt[62], Reuss[63], and Hill[64] methods were used, and the computational results are presented in (SI-10). The Young's modulus, bulk modulus, and shear modulus of the Co-rich phase in BCC and s-BCC-Y are shown in Fig. 3f, which indicates the modulus increases after the Y doping, consistent with the results of
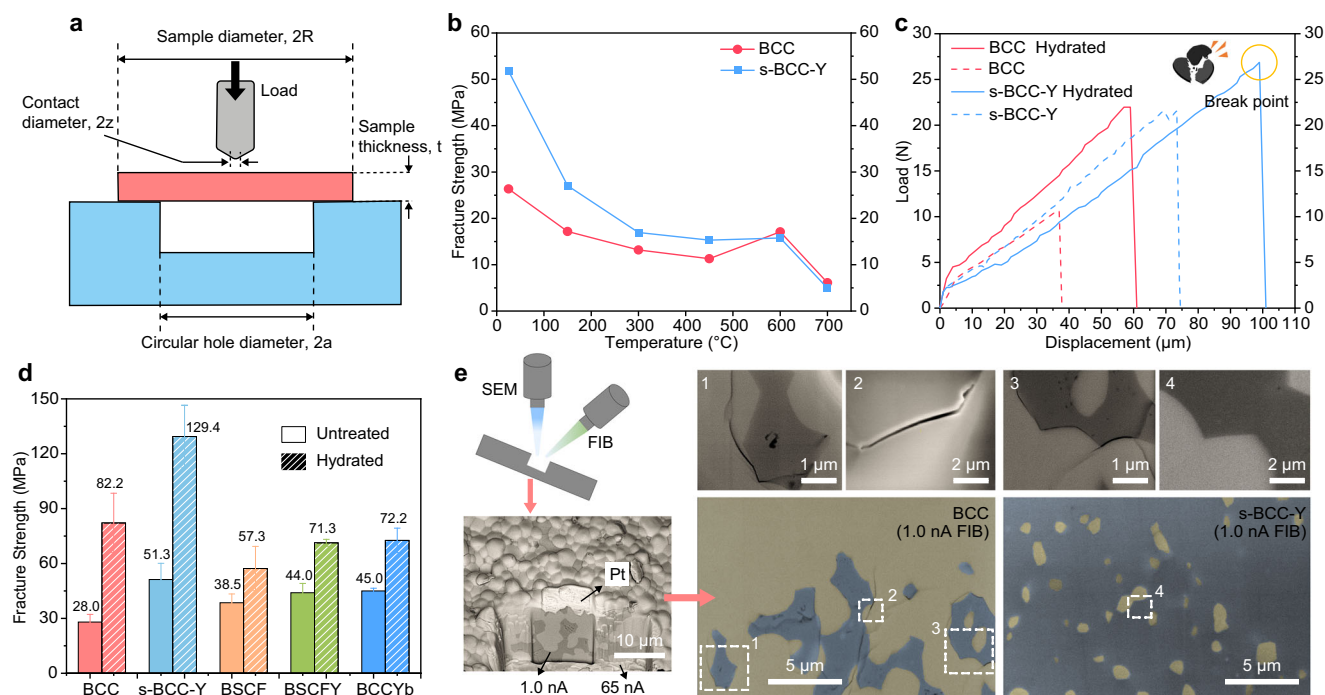
Fig. 4 | High-temperature fracture strength test and mechanistic analysis. a Ball on ring testing method fixture profile and annotations of calculation parameters. **b** Fracture strength test results from room temperature (28 °C) to high temperature (700 °C). **c** Load-displacement curve for the fracture strength test at 28 °C for BCC and s-BCC-Y, hydrated means the cathode specimen was conducted treatment with 10vol.% H_2O-air at 800 °C for 5 h. **d** Comparison of fracture strength before and after hydration for BCC, s-BCC-Y, BSCF, BSCFY, and s-BCC-Y cathode materials (Error bars represent standard deviation from the mean). **e** Observation of BCC and s-BCC-Y grain boundary by FIB-SEM. Source data for (**b**, **c**) were provided as a Source Data file.

nanoindentation tests. The Pugh's ratio (k = G/B) is often used to evaluate the quasi-ductile/brittle nature of ceramics[65,66]. When G/B is less than 0.571, it indicates a ductile property of the ceramic[67–69]. Both BCC and s-BCC-Y met Pugh's criterion, and s-BCC-Y (k = 0.511) had a lower k than BCC (k = 0.565). This suggests that s-BCC-Y has exhibited certain quasi-ductility characteristics, making it resistant to fracture. It is also consistent with the cathode fracture experiments we conducted next in Fig. 4.

Hydration-improved fracture stiffness at a macro-scale

To verify the positive effect of bulk stiffness enhancement on fracture strength, we examined the fracture strength of dense BCC and s-BCC-Y pellets using a ball-on-ring fixture, a more reliable method for testing the strength of flat brittle specimens than traditional 3-point bending test[70], as depicted in Fig. 4a. The specific calculations for strength were shown in the method section (details in SI-11). Fracture strength from room temperature to 700 °C of both BCC and s-BCC-Y are illustrated in Fig. 4b that the highest value of 52.1 MPa was achieved for s-BCC-Y at room temperature, over 80% higher than that of pristine BCC (28 MPa). Interestingly, the enhancement in fracture strength was more pronounced at lower temperatures, while it became negligible at higher temperatures (>600 °C). We attribute this phenomenon to chemical hydration, which occurs predominantly below the hydration temperature turning point. As is well known, perovskite-based cathode materials undergo hydration during the cooling process[24], which can optimize grain contact interfaces and, in turn, increase material stiffness.

This trend coincides well with the discrepancy of TEC curves below 600 °C in Fig. 2a, implying that the enhanced hydration indeed altered the thermal mechanical behaviors, in terms of both TEC and fracture strength. Accordingly in Fig. 4c, the load vs. displacement

curves of BCC and s-BCC-Y specimens till fracture were both further enhanced if treated with a higher 10vol.%-H_2O wetted air at 800 °C for 5 h with subsequent cooling. All these experimental findings indicate that enhanced hydration resulted in the increase of fracture strength in s-BCC-Y.

To further elucidate the universality of the strategy of hydration induced for mechanical enhancement, we also compared the fracture strength of the classic single cubic phase cathode $Ba_{0.5}Sr_{0.5}Co_{0.8}Fe_{0.2}O_3$ (BSCF) and B-site 10% Y doped $Ba_{0.5}Sr_{0.5}(Co_{0.8}Fe_{0.2})_{0.9}Y_{0.1}O_3$ (noted as BSCFY with XRD profile shown in SI-12), before and after the full hydration (800 °C, 10 vol.%-H_2O in air, 5 h), which were shown in Fig. 4d. As it presented, Y-doping effectively enhanced the fracture strength of BSCF, both before and after full hydration, which means hydration is not limited to the composite BCC system but also applies to single-phase cubic perovskites. However, this improvement is less significant compared to that observed in BCC. There might be two reasons for that. First, the high fraction of Co and Fe in BSCF already results in high fracture of oxygen vacancy that the further doping of Y does not show significant improvement of hydration capacity, Second, the high reducibility of $Co^{3/4+}$ and $Fe^{3/4+}$ ions (absent in valence-fixed Y^{3+}) at high temperature is the origin of its large TEC (>20 × 10^{-6} K^{-1}), and thus large thermal stress between grains. That implies the high fraction of Co/Fe in BSCF than BCC could dominate the fracture strength, other than the hydration capacity. Besides, we also doped the Yb element into BCC (nominally $BaCo_{0.7}Ce_{0.15}Yb_{0.15}O_3$, noted as BCCYb with XRD profile shown in SI-12), which is also a trivalent dopant, creating oxygen vacancies for hydration, similar to the Y element. The BCCYb also showed improved strength than BCC (see Fig. 4d), further confirming that the enhanced hydration due to trivalent doping can enhance fracture strength.

To get further direct evidence of the improved stiffness for anti-crack formation, FIB-SEM was used to scrutinize the internal microstructures of BCC and s-BCC-Y by ion milling as depicted in Fig. 4e.
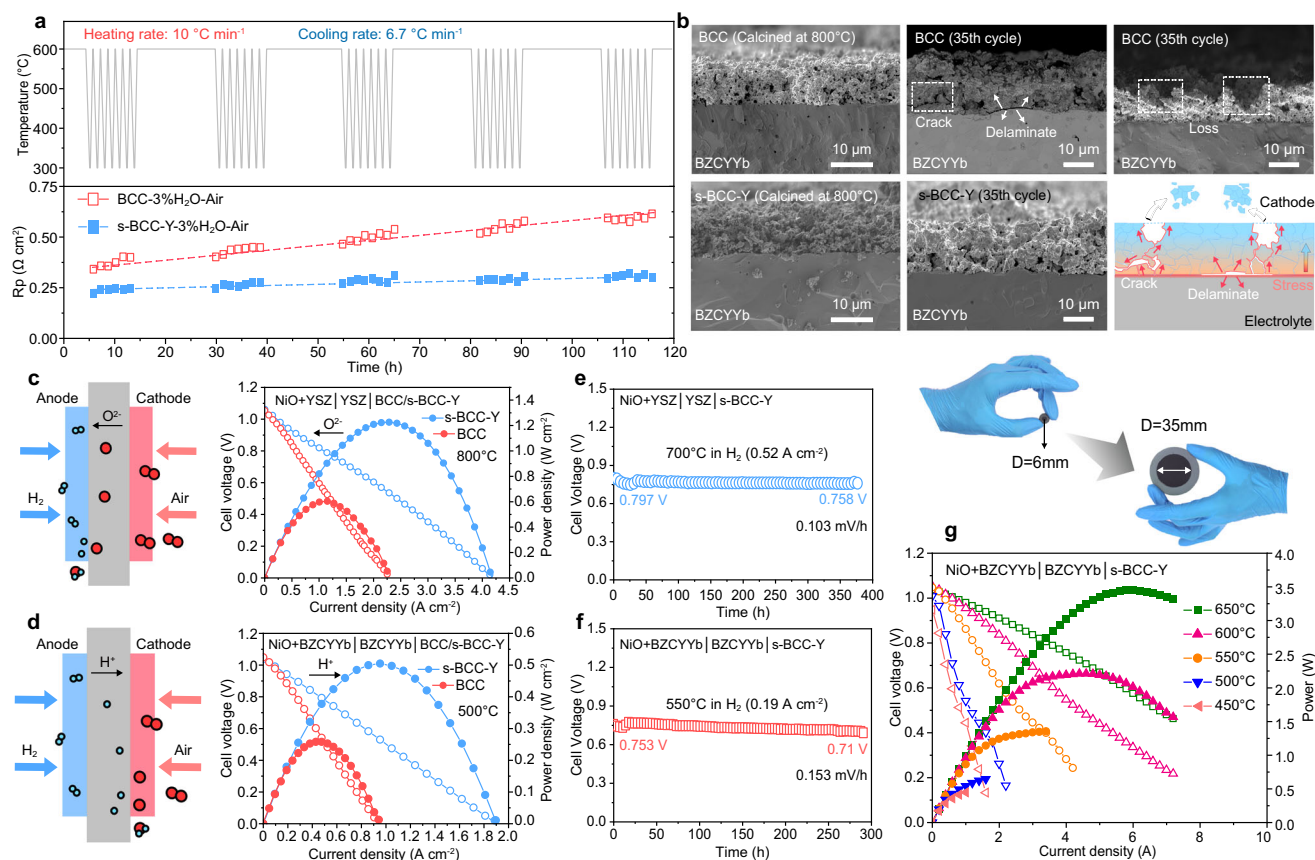
Fig. 5 | Electrochemical performance of thermal cycling and single cell stability.
a ASR(Rp) response of BCC and s-BCC-Y symmetric cell electrodes during 35 thermal cycles between 600 °C and 300 °C (at a heating rate of 10 °C min⁻¹ and cooling rate at about 6.7 °C min⁻¹) in air atmosphere. **b** Cross-sectional SEM and schematic diagram of a symmetric cell before and after cycling: crack, loss of the cathode, and delamination from electrolyte. I-V and I-P (I, current density; V, voltage; P, power density) curves of s-BCC-Y and BCC cathode with YSZ (**c**) and BZCYYb (**d**) electrolytes in H₂/air, at 800 and 500 °C, respectively. The stability curves of the fuel cells for s-BCC-Y cathode with YSZ(**e**) and BZCYYb electrolyte(**f**). **g** The power of a large-scale cell with an s-BCC-Y cathode diameter of 3.5 cm from 450 to 650 °C. Source data for (**a**, **c**–**g**) were provided as a Source Data file.

After sintering at 1150 °C for 5 h, the samples were naturally cooled to room temperature and then carefully transferred to the electron microscope for observation. There was an obvious distinction between BCC and s-BCC-Y. BCC displayed clear cracks along its phase boundaries and showed a tendency to propagate from their boundaries towards the interior of the grains. However, the s-BCC-Y showcased intimate intergranular contact, and almost no cracks were observed between the grain boundaries. Besides, a rapid quenching method was conducted to examine their crack resistance. Dense BCC and s-BCC-Y samples were quenched from high temperature (1150 °C) to RT, by direct taking the samples from furnace to the water (RT). which subjects the samples to rapid shrinkage and induces possible thermal cracks. As shown in the following surface (SI-13, Fig. S17), the cracks formed in the BCC sample were much more severe than the Y-doped samples, demonstrating the superior thermal shrinkage resistance of s-BCC-Y. This also correlates well with the interfacial observations at the lattice scale by TEM (in Fig. 1e, f). This difference of microstructures is solid evidence of the mechanism of stiffness enhancement as depicted in Fig. 1a due to the enlargement of the perovskite structure after Y-doping, leading to grain expansion countering the thermal shrinkage when cooled, which results in a closer contact between different grains.

As a short summary of the above mechanical assessment, a noticeable corelationship between enhancement in stiffness/fracture strength and hydration successfully demonstrated the effectiveness of facile Y-doping for developing mechanical robust cathode of SOFCs.

Electrochemical evaluation of hydrated s-BCC-Y during thermal cycling

The electrochemical activity and thermal-mechanical durability of s-BCC-Y as an oxygen-reduction electrode were evaluated. First, electrochemical impendence spectroscopy (EIS) measurements of BCC and s-BCC-Y symmetrical cells with BZCYYb electrolyte were performed under open-circuit conditions from 500 to 700 °C in ambient air atmosphere. The Arrhenius plots and Nyquist plots of the area-specific resistance (ASR, noted as Rp) of BCC and s-BCC-Y were compared in SI-14, Fig. S18. s-BCC-Y demonstrated consistently lower polarization resistance at all temperatures than BCC. For example, the Rp of s-BCC-Y was only 0.23 Ω cm², 28.1% lower than that of BCC (0.32 Ω cm²). The DRT analysis (SI-14, Fig. S18) shows the differences between BCC and s-BCC-Y are mainly observed at mid- and high-frequencies, suggesting that s-BCC-Y has a better oxygen ion conductivity and redox catalytic activity. The stability of the Rp of symmetric cells at OCV was also tested. After 300 h, the Rp of BCC increased from 0.325 Ω cm² to 0.71 Ω cm², showing a degradation of 1.28 mΩ cm²/h, while the decay of s-BCC-Y's is only 0.58 mΩ cm²/h (SI-14, Fig. S19). More importantly, s-BCC-Y demonstrated a much improved thermal cyclability of Rp, as shown in Fig. 5a. After 35 cycles (for ~120 h) of rapid temperature cycling between 300-600 °C, the Rp value of the s-BCC-Y electrode only slightly increased from 0.23 to 0.33 Ω cm², while BCC increased from 0.34 to 0.59 Ω cm² by almost 2 times (corresponding Nyquist plots and DRT shown in SI-14, Fig. S20). DRT analysis reveals that the main difference between the two occurs at low-frequency, indicating that slow processes, such as

gas diffusion within the BCC cathode, begin to change, likely due to interfacial delamination or electrode fracture. In contrast, s-BCC-Y shows smaller changes at low frequencies. Besides, a long-term stable cathode also needs to have good CO_2 resistance[71], and s-BCC-Y exhibited that better (see SI-15, Fig. S21). DRT results show significant enlargement of peaks in the low-frequency region of s-BCC-Y and BCC, which indicates that gas diffusion is suppressed, likely due to cathode surface carbonization and the coverage of carbonates impeding oxygen diffusion.

We examined the SEM morphology of BCC and s-BCC-Y before and post-cycling (Fig. 5b). As anticipated, not only delamination but also bulk crack (leads to the loss of partial cathode in the bulk) were observed in the BCC sample post-cycling. As illustrated in the schematic diagram (Fig. 5b), we attribute the extensive cathode loss observed after long-term cycling to fractures caused by thermal stress at the interface of a low-stiffness cathode. By contrast, the improved stiffness and fracture strength enabled s-BCC-Y to retain its intact porous framework without any delamination and bulk cracks, which is key to superior durability. In addition, it should be mentioned that no reactions were observed for both air electrodes and BZCYYb (SI-16, Fig. S24), Further confirming that the cracking and delamination observed at the interface were mainly caused by poor stiffness and thermo-mechanical properties in this work, rather than chemical side reactions.

To fully demonstrate the concept of chemically induced expansion offset as a general method for thermal-mechanical enhancement, we further tested s-BCC-Y as the cathode in both oxygen ion and proton-conducting single cells (SOFC and PCFC), using H_2 as the fuel. In Fig. 5c, d, the s-BCC-Y cathode reaches $1220 \, mW \, cm^{-2}$ at 800 °C, using NiO-YSZ as anode and YSZ as electrolyte, greatly outperforming the BCC cathode (only $603 \, mW \, cm^{-2}$ at 800 °C). On the NiO-BZCYYb| BZCYYb half-cell, s-BCC-Y also showed a better power density than BCC ($504 \, mW \, cm^{-2}$ vs. $258 \, mW \, cm^{-2}$ at 500 °C, This more significant improvement of performance in PCFC than SOFC can be explained by the more harsh thermal mechanical environment in PCFC than SOFC, that was resulted by the lower TEC of BZCYYb than YSZ[72,73]. Meanwhile, the long-term stability of single cells was also assessed. Both cells were able to sustain a consistent power output over an extended duration. In Fig. 5e, the cell output shows a voltage drop from 0.797 V to 0.758 V after 380 hours, corresponding to a 0.103 mV/h degradation. In Fig. 5f, the voltage decreases from 0.753 V to 0.71 V, representing a 0.153 mV/ h degradation. This strongly suggests that the s-BCC-Y composite cathode, improved by stiffness enhancement, exhibits remarkable performance in single fuel cells. This also indicates that the cathode, with enhanced hydration demonstrates good durability in both SOFC and PCFC configurations.

Finally, we further assessed the performance of s-BCC-Y on large-scale PSOFC (NiO-BZCYYb|BZCYYb|s-BCC-Y) with an active cathode area of $9.62 \, cm^2$, that is above 35 times higher than button cell testing (~$0.28 \, cm^2$) as compared in Fig. 5g. Considering cathode with a larger area is more vulnerable to cracking and delamination failures caused by the higher thermal stress in the multi-layered film due to geometry effect and strong local joule heating effect, the high large single cell performance of s-BCC-Y (a total power of 3.5 W at 650 °C, corresponding to a practical power density of ~$0.36 \, W/cm^{-2}$) again confirms its good thermo-mechanical robustness.

Discussions

Thermo-mechanical performance of air electrodes, including interface delamination and bulk crack are critical limiting factors for the robustness of SOFCs during thermal cycling. Many efforts have been made to solve the TEC mismatch problem between cathode and electrolyte. However, the insufficient fracture strength of bulk air electrodes, which dictates the bulk crack issues, has been overlooked for long.

This study indicates that material engineering techniques, such as acceptor-doping (with Y being one example, but not the only option), can enhance the material's hydration ability. This improved hydration, along with the associated "chemical expansion", significantly impacts the material's thermal expansion and stiffness under temperature fluctuations, which are typical in high-temperature fuel cells. Although the difference in TEC between s-BCC-Y and other materials like BZCYYb or YSZ remains substantial, even small enhancement of hydration ability can greatly improve the mechanical properties of the cathode material, especially its resistance to cracking. This improvement in anti-cracking behavior is the main factor contributing to the observed increase in mechanical robustness, taking slight degradation and enhanced long-term stability during extended thermal cycling tests.

This work highlights the critical role of cathode fracture in long-term cycling stability and proposes a simple, feasible hydration method to enhance the material's fracture stiffness. We believe this approach will not only improve the long-term stability of SOFCs but also offer an economically viable strategy for developing high-durability, high-stability, and high-performance cathodes. Furthermore, the scalability of this method is straightforward, with minimal impact on manufacturing costs, making it a promising solution for large-scale industrial applications.

Methods
Powder preparation
All perovskite materials in this paper, including $BaCo_{0.7}Ce_{0.3}O_{3\text{-delta}}$, $BaCo_{0.7}Ce_{0.15}Y_{0.15}O_{3\text{-delta}}$, BZCYYb, YSZ were prepared via a complexing sol-gel method. For instance, when preparing $BaCo_{0.7}Ce_{0.15}Y_{0.15}O_{3\text{-delta}}$, stoichiometric amounts of $Ba(NO_3)_2$-99.5%, $Co(NO_3)_2 \cdot 6H_2O$-99.9%, $Ce(NO_3)_3 \cdot 6H_2O$-99.95% and $Y(NO_3)_3 \cdot 6H_2O$-99.99% according to the nominal composition, were dissolved into water and heated at 180 °C under stirring. Ethylenediaminetetraacetic acid (EDTA-99.99%) and citric acid (CA-99.5%) were added to act as complexing agents at a molar ratio of 1:1:2 for total metal ions, EDTA and CA. $NH_3 \cdot H_2O$ was used to adjust the PH value of water in the solution to around 7. A sol-gel precursor was obtained after the removal of water in the solution by evaporation, which was pre-decomposed at 180 °C for 8 h to obtain the precursors. The as-synthesized precursors were then calcined at 1000 °C for 5 h in air to obtain the final product. The SEM is shown in SI-17. All materials mentioned above were procured from Aladdin Scientific Corporation.

Fabrication of symmetric cells and single cells
Symmetrical cells with the configuration of cathode|BZCYYb|cathode were fabricated for the electrochemical impedance spectroscopy (EIS) test. First, the as-synthesized BZCYYb powders were drily pressed into pellets and calcined at 1450 °C to obtain dense pellets, placed in a normal environment for standby use (~25 °C, 60% relative humidity). Next, the cathode suspension, consisting of the 1 g as-synthesized cathode materials, 0.8 ml glycerol, 2 ml ethylene glycol, and 10 ml isopropyl alcohol, was prepared by ball milling for 40 min. The suspension was sprayed onto both sides of BZCYYb disks and calcined at 800 °C for 2 h in air. On both sides of the cathode, silver paste was applied to create silver grids for the current collection, and silver wires were used to connect the cell and the electrochemical workstation for the needed test.

NiO+BZCYYb anode-supported single cells with thin-film electrolytes were prepared by dry-pressing and high-temperature co-sintering. Anode powders consisting of 6 g NiO, 4 g BZCYYb, 1 g starch, and appropriate ethanol were prepared by ball milling. Then, manually mixed and left to dry at room temperature. First, 0.35 g anode powder was pressed into a pellet with a pressure of 4 MPa, and the 0.02 g BZCYYb electrolyte was evenly spread on the anode surface and co-pressed under a pressure of 8 MPa. Then the bi-layer BZCYYb electrolyte disk was calcined at 1450 °C for 5 h in air. Finally, the cathode

suspension was sprayed onto the electrolyte surface with an effective area of 0.27 cm^{-2} and calcined at 800 °C for 2 h. The final thickness of the electrolyte layer is about 10 μm (See SI-17 for details). Regarding the large area single cell with a cathode area of 9.62 cm^2, the anode is prepared by casting processing, followed by spin-coating the electrolyte on the hot-pressed anode, co-sintering at 1450 °C to obtain the test half-cell and the cathode is sprayed onto the electrolyte surface too. The oxygen ion conducting SOFC with NiO-YSZ|YSZ half cells are purchased from Ningbo SOFCMAN company, with a 400μm NiO-YSZ anode, 15μm YSZ electrolyte, 3μm GDC barrier layer.

Material characterizations

The crystal structures of BCC and s-BCC-Y were carried out by Rigaku Miniflex 600 X-ray diffractometer (XRD) with Cu source. The diffraction patterns were collected in the 2-theta range between 10 and 80° with intervals of 0.02° at a scanning rate of 2°min^{-1}, Rietveld refinement was performed using jade and X'Pert HighScore plus software. The morphology of the cathode particles and fuel cell cross-section were investigated by Thermo Scientific Scios 2 scanning electron microscopy (SEM). A further micro-structure of s-BCC-Y was investigated using transmission electron microscopy (TEM, FEI Talos F200x). energy-dispersive X-ray spectroscopy (EDX) measurements were performed in the same instrument. XPS measurement were conducted with a spectrometer (Thermo Scientific K-Alpha). About 100 mg of cathode materials were pressed into a pellet on a sample holder. The sample was then introduced into the analysis chamber when the pressure was below 2.0×10^{-7} mbar. The spot size was set to 400 μm, operating at 12 kV and a filament current of 6 mA. Full-spectrum scans employed pass energy of 150 eV with a 1 eV step size, while narrow-scan spectra used a pass energy of 50 eV with a 0.1 eV step size. The experimental data peak fitting was performed using the software Avantage.

Electrochemical measurements

The I-V and I-P curves of cells were obtained using a Keithley 2460 source meter with a four-probe configuration. The anode of a single cell was fed by H$_2$ fuel with a flow rate of 80 ml min^{-1}, while the cathode was exposed to ambient air. The impedance of single and symmetrical cells was investigated by the EIS measurement by the Princeton electrochemical workstation (auto calibration) at open circuit voltage (OCV) conditions. The frequency of the EIS measurement ranged from 0.01 to 100,000 Hz and the single amplitude was 100 mV. During the testing process, the temperature was first raised to the maximum operating condition temperature, and then gradually decreased to conduct the I–V curve tests at subsequent temperatures. Taking the cell performance test in Fig. 5g as an example, after securing the cell in the fixture, H$_2$ fuel with a flow rate of 80 ml min^{-1} was introduced to the anode side. The temperature was then increased from room temperature to 650 °C at a rate of 10 °C/min, held for 10 min, and the testing began. Subsequently, the temperature was naturally decreased in intervals of 50 °C, with holding and testing conducted at each operating temperature, until the testing concluded at 450 °C.

Fracture strength testing

The fracture strength tests were conducted using a high-temperature mechanic testing machine (OTF-1500X-S-CR, Hefei Kejing, China). The fixture consists of a spherical punch and a circular sample holder with an internal ring. The sample holder, is made of pressureless sintered SiC, which is suitable for high-temperature testing, and is placed on a high-precision pressure sensor for accurate measurements. Several studies[74,75] have used a verified formula method to calculate the fracture strength (σ), the test profile and calculation parameter are shown in Fig. 4a. The formula (1) is used to calculate the fracture strength of

the material,

$$\sigma = \frac{A \times F}{t^2} \tag{1}$$

where t is the specimen thickness, F is the applied force, and A is a dimensionless factor that depends on the geometry of the specimen and loading ball, the ring diameter, and Poisson's ratio of the loading ball and test material. The factor A is calculated using Eq. 2 for this test,

$$A = \frac{3}{4 \times \pi}\left[\left(2(1+v_s) \times \ln\frac{a}{b}\right) + \frac{(1-v_s)\left(2a^2 - b^2\right)}{2R^2} + (1+v_s)\right] \tag{2}$$

where v_s is the Poisson's ratio of the test material, a is the radius of the support ring, R is the radius of the test specimen, and b is the contact radius of the loading ball. The contact radius of the loading ball b can be simplified to b = t/3 in this test.

The punch approach speed was 3 mm/min, and the approach threshold (the punch contact with the sample) was set to 0.05 kg. After contact, the approach speed was reduced to 0.1 mm/min until the cathode sample fractured. During high-temperature testing, the chamber's temperature was increased at a rate of 10 °C /min, in a vacuum environment and cooled by 25 °C circulating water. To eliminate experimental variability, each kind of sample underwent 20 trials at room temperature and 10 trials at high temperature. Data within the (μ-σ, μ+σ) confidence interval, about 65% confidence, were considered valid, and the average of these valid data was accepted in this paper.

Nanoindentation testing

This test was performed using the Bruker Hysitron PI 89 Picoindenter. High-temperature Berkovich Probe (diamond, Half Angle 65.27°, Included Angle 142.30°, C$_0$ 24.5, Young's modulus 1140 GPa, Poisson's ratio 0.07) and Cube Corner probe (diamond, Half Angle 35.26°, Included Angle 90°, C$_0$ 2.598, Young's modulus 1140 GPa, Poisson's ratio 0.07) were used to test.

The linear fitting models proposed by Doerner and Nix[76] and exponential fitting models proposed by Oliver and Pharr[56,57] are used to calculate equivalent elastic modulus Er,

$$E_r = \frac{\sqrt{\pi}}{2\sqrt{A}} \times S \tag{3}$$

Where S is the initial unloading slope, and A represents the contact area between the probe and the material. The contact area A is determined using the Oliver-Pharr method by relating it to the contact depth h$_C$, where A = F(h$_C$), and h$_C$ is given by:

$$h_c = h_{max} - \varepsilon\frac{P_{max}}{S} \tag{4}$$

Where h_{max} is the maximum displacement during testing, ε is a geometric parameter depending on the shape of the indenter. Then, Young's modulus of materials was obtained by:

$$\frac{1}{E_r} = \frac{1-v_1^2}{E_1} + \frac{1-v_2^2}{E_2} \tag{5}$$

Where E$_1$ and v_1 are the Young's modulus and Poisson's ratio of the tested material, E$_2$ and v_2 are the Young's modulus and Poisson's ratio of the testing probe material. The hardness H was calculated by:

$$H = \frac{P_{max}}{A} \tag{6}$$

where P_{max} is the maximum load applied, and A is the contact area between the indenter and the tested material.

The probe approach speed was 150 nm/s, and the approach threshold was 50 μN. Once the probe reached a depth of 1500 nm, it remained at this depth for 10 s, and then the probe withdrew at a speed of 150 nm/s. During high-temperature testing, the chamber's temperature was increased at a rate of 30 °C /min in a vacuum environment and cooled by 25 °C circulating water. To eliminate experimental variability, each kind of sample underwent 150 trials at room temperature (25 °C) and 100 trials at high temperature (150–700 °C). Data within the (μ-σ, μ+σ) confidence interval, about 65% confidence, were considered valid, and the average of these valid data was accepted in this paper.

Numerical simulations
The interface thermal stress numerical simulation was conducted by COMSOL Multiphysics 5.5, and the model was built by actual SEM porous cathode-dense electrolyte interface characteristics. Mesh independence analysis was conducted for all simulations, and unstructured grids were employed. The detailed process is presented in the SI-5.

DFT computations
The TEC was calculated by Ab initio Car-Pareinello molecular dynamics (AIMD) within the framework of DFT. The exchange-correlation term was determined using the generalized gradient approximation (GGA) within the Beke-Lee-Yang-Parr (BLYP) implementation[77,78]. Norm-conserving pseudopotentials were used, with s and p as nonlocal orbitals and d as local orbitals. The AIMD calculations were performed using the SIESTA code, which is based on a flexible linear combination of atomic orbitals (LCAO) basis sets[79] and boasts efficient Order-N scaling[80]. A cutoff radius of 250 Ry was employed to ensure that the self-consistent procedure converged to less than 1 meV/atom. During atomic relaxation, a maximum of 25 electronic steps were used for each ionic step. For molecular dynamics, the Parinello-Rahman method[81] with variable shape and volume of the unit cell was applied (NPT ensemble). A $3 \times 3 \times 3$ supercell was built based on the optimized unit cell in different temperatures. Monkhorst-Pack ($2 \times 2 \times 2$) was set for Brillouim zone sampling. The temperature range investigated was T = 600K–1000 K, with increments of $\Delta T = 100$ K for the SIESTA calculations. Finally, the TEC of the structure was calculated using the Phonopy software through the quasi-harmonic approximation (QHA) method.

The modulus calculations were conducted using VASP, employing plane-wave basis sets and the projector augmented-wave method. We utilized the generalized gradient approximation (GGA) with the Perdew-Burke-Ernzerhof (PBE) parametrization[82] for the exchange correlation potential. The energy cutoff was set to 500 eV, and the Brillouin-zone integration was performed using a Γ-centered Monkhorst-Pack mesh[83] of $3 \times 3 \times 3$ for $BaCoO_3$ and $5 \times 5 \times 2$ for $BaCeO_3$, as implemented by VASPKIT[84]. The structural optimizations were carried out until the maximum force on each atom reached less than 0.01 eV/Å, and the energy convergence criterion was set to 10^{-8} eV. We set seven different strains with a range of −0.015 to 0.015 and a step size of 0.005. The elastic tensor matrices for different structures were calculated, and the Young's modulus (Y), bulk modulus (B), and shear modulus (G) of the structures were obtained using the Voigt, Reuss, and Hill methods.

Data availability
The all data in this article can be accessed within the main text, supplementary materials, and responses to reviewers' comments. All source data are provided with this paper. Additional data are available upon request from the first author or the corresponding author. Source data are provided with this paper.

References
1. Duan, C. et al. Highly durable, coking and sulfur tolerant, fuel-flexible protonic ceramic fuel cells. *Nature* **557**, 217–222 (2018).
2. Boldrin, P. & Brandon, N. P. Progress and outlook for solid oxide fuel cells for transportation applications. *Nat. Catal.* **2**, 571–577 (2019).
3. Zhang, Y. et al. Thermal-expansion offset for high-performance fuel cell cathodes. *Nature* **591**, 246–251 (2021).
4. Shin, J. F. et al. Self-assembled dynamic perovskite composite cathodes for intermediate temperature solid oxide fuel cells. *Nat. Energy* **2**, 1–7 (2017).
5. Song, Y. et al. A cobalt-free multi-phase nanocomposite as near-ideal cathode of intermediate-temperature solid oxide fuel cells developed by smart self-assembly. *Adv. Mater.* **32**, 1906979 (2020).
6. Seong, A., Jeong, D., Kim, M., Choi, S. & Kim, G. Performance comparison of composite cathode: mixed ionic and electronic conductor and triple ionic and electronic conductor with $BaZr_{0.1}Ce_{0.7}Y_{0.1}Yb_{0.1}O_{3-\delta}$ for highly efficient protonic ceramic fuel cells. *J. Power Sour.* **530**, 231241 (2022).
7. Wang, M. S. et al. A novel composite cathode $La_{0.6}Sr_{0.4}CoO_{3-\delta}$-$BaZr_{0.1}Ce_{0.7}Y_{0.1}Yb_{0.1}O_{3-\delta}$ for intermediate temperature solid oxide fuel cells. *Ceram. Int.* **41**, 5017–5025 (2015).
8. Wang, K. et al. Properties and performance of $Ba_{0.5}Sr_{0.5}Co_{0.8}Fe_{0.2}O_{3-\delta}$+$Sm_{0.2}Ce_{0.8}O_{1.9}$ composite cathode. *J. Power Sour.* **179**, 60–68 (2008).
9. Heidari, D., Javadpour, S. & Chan, S. H. Optimization of BSCF-SDC composite air electrode for intermediate temperature solid oxide electrolyzer cell. *Energy Convers. Manag.* **136**, 78–84 (2017).
10. Kim, J.-D. et al. Characterization of LSM-YSZ composite electrode by ac impedance spectroscopy. *Solid State Ion.* **143**, 379–389 (2001).
11. Lu, F. et al. Application of a negative thermal expansion oxide in SOFC cathode. *Ceram. Int.* **47**, 1095–1100 (2021).
12. Ghatee, M., Shariat, M. & Irvine, J. T. S. Investigation of electrical and mechanical properties of 3YSZ/8YSZ composite electrolytes. *Solid State Ion.* **180**, 57–62 (2009).
13. Lipinska-Chwalek, M., Malzbender, J., Chanda, A., Baumann, S. & Steinbrech, R. Mechanical characterization of porous $Ba_{0.5}Sr_{0.5}Co_{0.8}Fe_{0.2}O_{3-d}$. *J. Eur. Ceram. Soc.* **31**, 2997–3002 (2011).
14. Chou, Y. S., Stevenson, J. W., Armstrong, T. R. & Pederson, L. R. Mechanical properties of $La_{1-x}Sr_xCo_{0.2}Fe_{0.8}O_3$ mixed-conducting perovskites made by the combustion synthesis technique. *J. Am. Ceram. Soc.* **83**, 1457–1464 (2000).
15. Zhu, J. H. & Ghezel-Ayagh, H. Cathode-side electrical contact and contact materials for solid oxide fuel cell stacking: a review. *Int. J. Hydrog. Energy* **42**, 24278–24300 (2017).
16. Giraud, S. & Canel, J. Young's modulus of some SOFCs materials as a function of temperature. *J. Eur. Ceram. Soc.* **28**, 77–83 (2008).
17. Yoshimura, H. N. et al. Relationship between elastic and mechanical properties of dental ceramics and their index of brittleness. *Ceram. Int.* **38**, 4715–4722 (2012).
18. Medvedev, D. et al. $BaCeO_3$: materials development, properties and application. *Prog. Mater. Sci.* **60**, 72–129 (2014).
19. Iwahara, H., Uchida, H., Ono, A. K. & Ogaki, K. Proton conduction in sintered oxides based on $BaCeO_3$. *J. Electrochem. Soc.* **135**, 529 (1988).
20. Andersson, A. K., Selbach, S. M., Knee, C. S. & Grande, T. Chemical expansion due to hydration of proton-conducting perovskite oxide ceramics. *J. Am. Ceram. Soc.* **97**, 2654–2661 (2014).
21. Suntsov, A. Y., Politov, B., Leonidov, I., Patrakeev, M. & Kozhevnikov, V. Improved stability and defect structure of yttrium doped cobaltite $PrBaCo_2O_{6-\delta}$. *Solid State Ion.* **295**, 90–95 (2016).
22. Unger, L.-S. et al. Yttrium doping of $Ba_{0.5}Sr_{0.5}Co_{0.8}Fe_{0.2}O_{3-\delta}$ part I: influence on oxygen permeation, electrical properties, reductive stability, and lattice parameters. *J. Eur. Ceram. Soc.* **38**, 2378–2387 (2018).

23. Duan, C. et al. Readily processed protonic ceramic fuel cells with high performance at low temperatures. *Science* **349**, 1321–1326 (2015).

24. Chen, T. et al. Toward durable protonic ceramic cells: hydration-induced chemical expansion correlates with symmetry in the Y-doped $BaZrO_3$-$BaCeO_3$ solid solution. *J. Phys. Chem. C.* **125**, 26216–26228 (2021).

25. Kim, H.-S., Bae, H. B., Jung, W. & Chung, S.-Y. Manipulation of nanoscale intergranular phases for high proton conduction and decomposition tolerance in $BaCeO_3$ polycrystals. *Nano Lett.* **18**, 1110–1117 (2018).

26. Cheng, E. J., Sharafi, A. & Sakamoto, J. Intergranular Li metal propagation through polycrystalline $Li_{6.25}Al_{0.25}La_3Zr_2O_{12}$ ceramic electrolyte. *Electrochim. Acta* **223**, 85–91 (2017).

27. Kim, H.-S., An, J.-S., Bae, H. B. & Chung, S.-Y. Atomic-scale observation of premelting at 2D lattice defects inside oxide crystals. *Nat. Commun.* **14**, 2255 (2023).

28. Shannon, R. D. Revised effective ionic radii and systematic studies of interatomic distances in halides and chalcogenides. *Acta Crystallogr. Sect. A* **32**, 751–767 (1976).

29. Han, D., Hatada, N. & Uda, T. Chemical expansion of yttrium-doped barium zirconate and correlation with proton concentration and conductivity. *J. Am. Ceram. Soc.* **99**, 3745–3753 (2016).

30. Hudish, G., Manerbino, A., Coors, W. G. & Ricote, S. Chemical expansion in $BaZr_{0.9-x}Ce_xY_{0.1}O_{3-\delta}$ (x= 0 and 0.2) upon hydration determined by high-temperature X-ray diffraction. *J. Am. Ceram. Soc.* **101**, 1298–1309 (2018).

31. Liu, Z. et al. Synergistic dual-phase air electrode enables high and durable performance of reversible proton ceramic electrochemical cells. *Nat. Commun.* **15**, 472 (2024).

32. Song, Y. et al. Self-assembled triple-conducting nanocomposite as a superior protonic ceramic fuel cell cathode. *Joule* **3**, 2842–2853 (2019).

33. Gao, Y. et al. Self-assembled composite cathodes with TEC gradient for proton-conducting solid oxide fuel cells. *Adv. Function. Mater.* https://doi.org/10.1002/adfm.202416625 (2024).

34. Aguadero, A. et al. Structural and electrical characterization of the novel $SrCo_{0.9}Sb_{0.1}O_{3-\delta}$ perovskite: evaluation as a solid oxide fuel cell cathode material. *Chem. Mater.* **19**, 6437–6444 (2007).

35. Ding, X. et al. Cation deficiency enabled fast oxygen reduction reaction for a novel SOFC cathode with promoted CO_2 tolerance. *Appl. Catal. B: Environ.* **243**, 546–555 (2019).

36. Niu, B. et al. First-principles study of the anisotropic thermal expansion and thermal transport properties in h-BN. *Sci. China Mater.* **64**, 953–963 (2021).

37. Wang, X. et al. An insight into the effects of transition metals on the thermal expansion of complex perovskite compounds: an experimental and density functional theory investigation. *Phys. Chem. Chem. Phys.* **20**, 17781–17789 (2018).

38. Liu, J. et al. Synergistic electron doping and ion conductive phase incorporating of $SrCoO_{3-\delta}$ as desirable cathode materials for intermediate-temperature solid oxide fuel cells. *Ceram. Int.* **46**, 28332–28341 (2020).

39. Zhai, S. et al. A combined ionic Lewis acid descriptor and machine-learning approach to prediction of efficient oxygen reduction electrodes for ceramic fuel cells. *Nat. Energy* **7**, 866–875 (2022).

40. Kuklja, M., Kotomin, E. A., Merkle, R., Mastrikov, Y. A. & Maier, J. Combined theoretical and experimental analysis of processes determining cathode performance in solid oxide fuel cells. *Phys. Chem. Chem. Phys.* **15**, 5443–5471 (2013).

41. Pauling, L. The dependence of bond energy on bond length. *J. Phys. Chem.* **58**, 662–666 (1954).

42. Gordy, W. Dependence of bond order and of bond energy upon bond length. *J. Chem. Phys.* **15**, 305–310 (1947).

43. Phillips, J. Ionicity of the chemical bond in crystals. *Rev. Mod. Phys.* **42**, 317 (1970).

44. Brown, I. T., & Shannon, R. D. Empirical bond-strength-bond-length curves for oxides. *Acta Crystallogr. Sect. A* **29**, 266–282 (1973).

45. Zhao, H. et al. Investigation of mixed conductor $BaCo_{0.7}Fe_{0.3-x}Y_xO_{3-\delta}$ with high oxygen permeability. *J. Phys. Chem. C.* **114**, 17975–17981 (2010).

46. Yang, G. et al. Toward reducing the operation temperature of solid oxide fuel cells: our past 15 years of efforts in cathode development. *Energy Fuels* **34**, 15169–15194 (2020).

47. Wang, X. et al. Enhanced proton conduction with low oxygen vacancy concentration and favorable hydration for protonic ceramic fuel cells cathode. *ACS Appl. Mater. Interfaces* **15**, 1339–1347 (2022).

48. Ji, Q., Bi, L., Zhang, J., Cao, H. & Zhao, X. S. The role of oxygen vacancies of ABO_3 perovskite oxides in the oxygen reduction reaction. *Energy Environ. Sci.* **13**, 1408–1428 (2020).

49. Hu, H. et al. Conductivities in Yttrium-Doped Barium Zirconate: a First-Principles Study. *Crystals* **13**, 401 (2023).

50. Wei, B. et al. Crystal structure, thermal expansion and electrical conductivity of perovskite oxides $BaxSr1-xCoO_{0.8}Fe0.2O_{3-\delta}$ (0.3≤ x≤ 0.7). *J. Eur. Ceram. Soc.* **26**, 2827–2832 (2006).

51. Yu, Z. et al. Superior durability and activity of a benchmark triple-conducting cathode by tuning thermo-mechanical compatibility for protonic ceramic fuel cells. *Adv. Funct. Mater.* **34**, 2309698 (2024).

52. Agun, L., Rahman, H. A., Ahmad, S. & Muchtar, A. Durability and stability of LSCF composite cathode for intermediate-low temperature of solid oxide fuel cell (IT-LT SOFC): short review. *Adv. Mater. Res.* **893**, 732–737 (2014).

53. Ahn, S.-m et al. Nanomechanical approach for flexibility of organic-inorganic hybrid perovskite solar cells. *Nano Lett.* **19**, 3707–3715 (2019).

54. Launey, M. E. & Ritchie, R. O. On the fracture toughness of advanced materials. *Adv. Mater.* **21**, 2103–2110 (2009).

55. Orlovskaya, N., Gogotsi, Y., Reece, M., Cheng, B. & Gibson, I. Ferroelasticity and hysteresis in $LaCoO_3$ based perovskites. *Acta Mater.* **50**, 715–723 (2002).

56. Oliver, W. C. & Pharr, G. M. Measurement of hardness and elastic modulus by instrumented indentation: advances in understanding and refinements to methodology. *J. Mater. Res.* **19**, 3–20 (2004).

57. Oliver, W. C. & Pharr, G. M. An improved technique for determining hardness and elastic modulus using load and displacement sensing indentation experiments. *J. Mater. Res.* **7**, 1564–1583 (1992).

58. Li, W., Wang, R., Li, D. & Fang, D. A model of temperature-dependent Young's modulus for ultrahigh temperature ceramics. *Phys. Res. Int.* **2011**, 791545 (2011).

59. Katz, R. N. High-temperature structural ceramics. *Science* **208**, 841–847 (1980).

60. Dukino, R. D. & Swain, M. V. Comparative measurement of indentation fracture toughness with Berkovich and Vickers indenters. *J. Am. Ceram. Soc.* **75**, 3299–3304 (1992).

61. Larsson, P.-L., Giannakopoulos, A., Söderlund, E., Rowcliffe, D. & Vestergaard, R. Analysis of Berkovich indentation. *Int. J. Solids Struct.* **33**, 221–248 (1996).

62. Chaudhuri, O. et al. Substrate stress relaxation regulates cell spreading. *Nat. Commun.* **6**, 6365 (2015).

63. Reuß, A. Berechnung der fließgrenze von mischkristallen auf grund der plastizitätsbedingung für einkristalle. *ZAMM-Journal Appl. Math. Mech./Z. f.ür. Angew. Mathematik und Mech.* **9**, 49–58 (1929).

64. Hill, R. The elastic behaviour of a crystalline aggregate. *Proc. Phys. Soc. Sect. A* **65**, 349 (1952).

65. Zhang, W. et al. High temperature mechanical and thermal properties of $Ca_xBa_{1-x}ZrO_3$ solid solutions. *Ceram. Int.* **46**, 17416–17422 (2020).

66. Pugh, S. XCII. Relations between the elastic moduli and the plastic properties of polycrystalline pure metals. *Lond. Edinb. Dublin Philos. Mag. J. Sci.* **45**, 823–843 (1954).

67. Zhou, Y., Xiang, H., Lu, X., Feng, Z. & Li, Z. Theoretical prediction on mechanical and thermal properties of a promising thermal barrier material: $Y_4Al_2O_9$. *J. Adv. Ceram.* **4**, 83–93 (2015).

68. Xu, Q. et al. Theoretical prediction, synthesis, and crystal structure determination of new MAX phase compound V_2SnC. *J. Adv. Ceram.* **9**, 481–492 (2020).

69. Niu, H. et al. Extra-electron induced covalent strengthening and generalization of intrinsic ductile-to-brittle criterion. *Sci. Rep.* **2**, 718 (2012).

70. Wagemans, H. Ball-on-ring test revisited. *J. Am. Ceram. Soc.* **72**, 1538–1541 (1989).

71. Liu, Z. et al. Towards high performance durable ceramic fuel cells using a triple conducting perovskite cathode. *Appl. Catal. B: Environ.* **346**, 123678 (2024).

72. Chen, J. et al. A novel layered perovskite Nd ($Ba_{0.4}Sr_{0.4}Ca_{0.2}$) $Co_{1.6}Fe_{0.4}O_{5+\delta}$ as cathode for proton-conducting solid oxide fuel cells. *J. Power Sour.* **428**, 13–19 (2019).

73. Mori, M., Yamamoto, T., Itoh, H., Inaba, H. & Tagawa, H. Thermal expansion of nickel-zirconia anodes in solid oxide fuel cells during fabrication and operation. *J. Electrochem. Soc.* **145**, 1374 (1998).

74. Lupercio, A. E. et al. Ball-on-ring test validation for equibiaxial flexural strength testing of engineered ceramics. *Int. J. Ceram. Eng. Sci.* **3**, 128–139 (2021).

75. Ban, S. & Anusavice, K. Influence of test method on failure stress of brittle dental materials. *J. Dent. Res.* **69**, 1791–1799 (1990).

76. Doerner, M. F. & Nix, W. D. A method for interpreting the data from depth-sensing indentation instruments. *J. Mater. Res.* **1**, 601–609 (1986).

77. Lee, C., Yang, W. & Parr, R. G. Development of the Colle-Salvetti correlation-energy formula into a functional of the electron density. *Phys. Rev. B* **37**, 785 (1988).

78. Becke, A. D. Density-functional exchange-energy approximation with correct asymptotic behavior. *Phys. Rev. A* **38**, 3098 (1988).

79. Sankey, O. F. & Niklewski, D. J. Ab initio multicenter tight-binding model for molecular-dynamics simulations and other applications in covalent systems. *Phys. Rev. B* **40**, 3979 (1989).

80. Ordejón, P. Order-N tight-binding methods for electronic-structure and molecular dynamics. *Comput. Mater. Sci.* **12**, 157–191 (1998).

81. Parrinello, M. & Rahman, A. Crystal structure and pair potentials: a molecular-dynamics study. *Phys. Rev. Lett.* **45**, 1196 (1980).

82. Perdew, J. P., Burke, K. & Ernzerhof, M. Generalized gradient approximation made simple. *Phys. Rev. Lett.* **77**, 3865 (1996).

83. Monkhorst, H. J. & Pack, J. D. Special points for Brillouin-zone integrations. *Phys. Rev. B* **13**, 5188 (1976).

84. Wang, V., Xu, N., Liu, J.-C., Tang, G. & Geng, W.-T. VASPKIT: a user-friendly interface facilitating high-throughput computing and analysis using VASP code. *Comput. Phys. Commun.* **267**, 108033 (2021).

Acknowledgements

Author contributions

H.Y. and Y.Z. conducted the majority of the experimental work, analyzed the data, and contributed to manuscript writing. Z.L. provided most of the experimental guidance, and J.L. supplied the large cells for testing purposes. C.H. conducted stability tests on the fuel cell. H.L. analyzed the XRD and TEM data. M.S. and M.N. provided suggestions to the laboratory, characterizations and numerical simulation. Z.S and B.C. provided critical and helpful suggestions for the experimental methods and contributed to manuscript writing. Y.Z., B.C., Z.S. and H.X. proposed and designed the concept. H.X. conceived the idea and supervised the research.

Competing interests

The authors declare no competing interests.

Additional information

Supplementary information The online version contains supplementary material available at https://doi.org/10.1038/s41467-025-57611-1.

Correspondence and requests for materials should be addressed to Yuan Zhang, Bin Chen, Zongping Shao or Heping Xie.

Peer review information *Nature Communications* thanks the anonymous, reviewer(s) for their contribution to the peer review of this work. A peer review file is available.

Reprints and permissions information is available at http://www.nature.com/reprints

Publisher's note Springer Nature remains neutral with regard to jurisdictional claims in published maps and institutional affiliations.